Structural strengthening and damage behaviors of hybrid sprayed fiber-reinforced polymer composites containing carbon fiber cores

SM Park[1], BJ Yang[2], BR Kim[3], SK Ha[4] and HK Lee[1]

Abstract
Recently, composite materials of a hybrid strategy are being developed to reduce the vulnerability of partial rupture failure. Simultaneously, the demand of a modelling method particularly for simulating the behavior of these materials is also emerging. This paper presents novel hybrid sprayed fiber-reinforced polymer composites containing carbon fiber cores developed for strengthening reinforced concrete structures, and a theoretical approach to model these materials. A micromechanical formulation that accounts for the hybrid characteristic of the composites was proposed to predict the overall performance of the composites. The derived model was then implemented into the nonlinear finite element codes to predict the structural behavior of the reinforced concrete beams retrofitted with the composites subjected to loading. A series of three-point bending tests of specimens were carried out to validate the predictability of the modeling technique. The obtained test results were comparatively explored with discussions of the theoretical approaches.

[1]Department of Civil and Environmental Engineering, Korea Advanced Institute of Science and Technology (KAIST), South Korea
[2]Multifunctional Structural Composite Research Center, Institute of Advanced Composite Materials, Korea Institute of Science and Technology (KIST), South Korea
[3]Civil and Architectural Engineering Group, KEPCO Engineering and Construction Company (KEPCO E&C), Inc., South Korea
[4]Department of Nuclear Safety Research, Korea Institute of Nuclear Safety (KINS), South Korea

SM Park and BJ Yang contributed equally to this work.

Corresponding author:
HK Lee, Department of Civil and Environmental Engineering, KAIST, 291 Daehak-ro, Yuseong-gu, Daejeon, Korea.
Email: haengki@kaist.ac.kr

Introduction

For decades, studies of strengthening and retrofitting deteriorated reinforced concrete (RC) structures with sprayed fiber-reinforced polymer (SFRP) composite materials have been extensively carried out, owing to its excellent engineering properties (Lee, 2004; Lee and Hausmann 2004; Lee et al., 2005, 2008a). Strengthening RC structures with SFRP utilizes fibers chopped into designated length and randomly oriented in the matrix, and can be applied by spraying the stream of both fibers and resin onto the substrate of concrete structures (Lee, 2004; Lee and Hausmann, 2004). The advantage of this technique includes its cost-effectiveness, easy and rapid installation, and more importantly, its capability to enhance the load capacity, ductility, and energy absorption capacity of the structure to significant extent (Lee et al., 2008a; Yang et al., 2014).

Recent studies of SFRP in the field of civil engineering are intensively focused on overcoming the identified obstacles which hinder the broad application of this technique. These studies are not limited to, but those deserve to be highlighted may include development of advanced spray multiple layup process for quality control of SFRP composite (Ha et al., 2015a), and improving the sag-resistance of SFRP system (Ha et al., 2015b). The spray multiple layup process proposed by Ha et al. (2015a) ensures the quality of the SFRP composites, i.e. consistent thickness and volume fractions of the fibers (Ha et al., 2015a). Moreover, the aspect of SFRP for practical applications in light of strengthening RC structures was thoroughly explored by assessing the sag-resistance (Ha et al., 2015b, 2015c) and bonding characteristic of SFRP composites from concrete (Ha et al., 2013).

On the other hand, SFRP composites bonded to RC beam are vulnerable to brittle failure, due to the locally concentrated stress induced by progressive crack in composites (Ha et al., 2015c). To overcome the premature failure of the strengthening material, the present study proposes novel hybrid SFRP composites, in which a carbon fiber (CF) core is embedded (hereafter, referred to as "hybrid SFRP composites"), as schematically illustrated in Figure 1(a). The anticipated effect of CF bundles incorporated in the SFRP matrix is that the RC beam strengthened with this material may persist to provide strength and ductility even after partial rupture failure of the composites. Hybridization of glass FRP sheets with carbon FRP has been explored in previous studies, which reported its synergistic effect on strengthening concrete structures (Choi et al., 2011; Kang, 2016; Kang et al., 2014).

In a theoretical view point, analytical and numerical techniques for evaluating the performance of the rehabilitation methods are being examined along with the extensive experimentations. The advantage of the theoretical approaches is that they are more expedient and economical in comparison with structural testing conducted in a laboratory (Ouaar et al., 2007). In particular, a combined micromechanics and finite element (FE) analysis has been proven for its capability of predicting the mechanical behavior of concrete strengthened with composite materials in many studies (Lee and Kim, 2007; Lee et al., 2005, 2008b; Nam et al., 2009; Yang et al., 2014). Despite the advances in understanding composite materials from theoretical perspectives, the progress and development of new hybrid composites have called for greater scientific knowledge. In particular, no material model which is capable of simulating the complex damage behavior of hybrid composites bonded to concrete is thus far proposed. Therefore, development of the material modeling for the new hybrid composites will emerge as the topic of many studies in future.

In this study, a novel method utilizing hybrid SFRP composites for strengthening RC beams, which are distinguished from the existing SFRP methods, is theoretically and experimentally studied. Micromechanical formulation (Ju and Chen, 1994; Lee et al., 2005; Yang et al., 2014) is derived to account for the proposed hybrid SFRP composites containing CF cores, and the principal scheme for modeling the hybrid SFRP is briefly described in Figure 1(b).
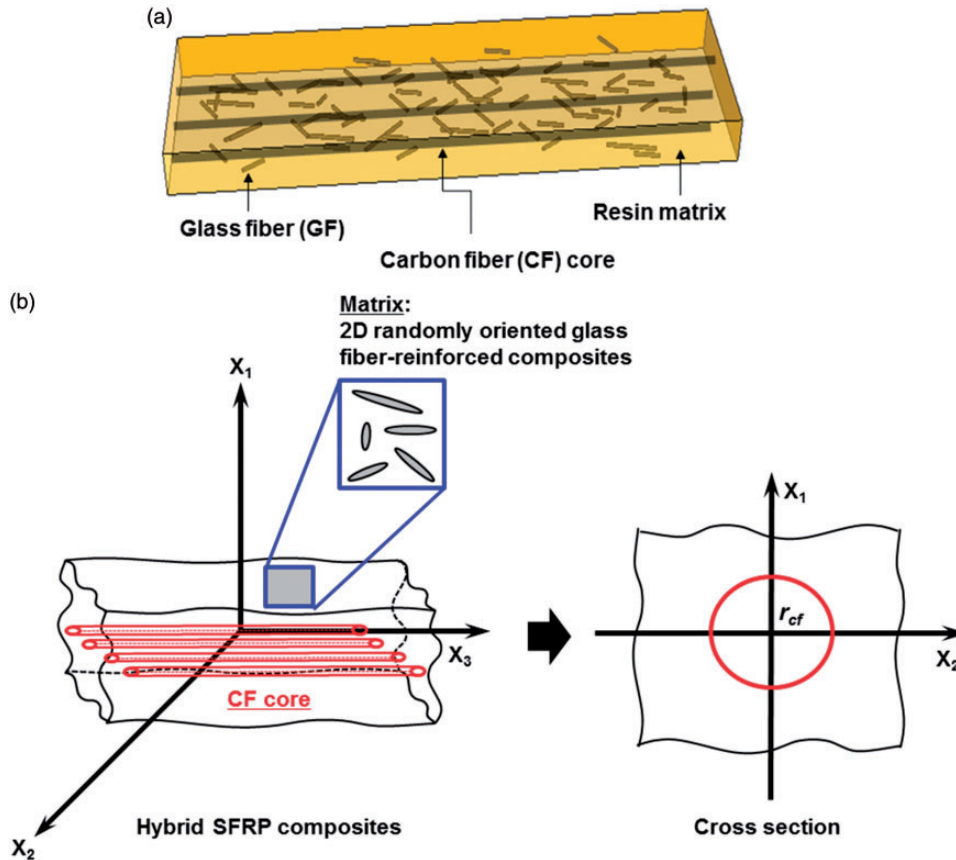
Figure 1. (a) Three-dimensional illustration and (b) schematic drawings of the hybrid SFRP composites.

The effectiveness of the proposed theoretical approaches is validated by comparing predictions with experimental results. Based on the method that involves a CF core in the SFRP laminate, the RC beams are strengthened with the SFRP composites containing CF bundles. Simultaneously, a series of three-point bending tests are conducted to investigate the flexural strengthening behavior of such system. The structural strengthening effect and damage behaviors in the three-point bending tests are estimated using the FE code in which the present micromechanics-based model is implemented. The results obtained by numerical approaches were comparatively explored with discussions of the experimentally obtained results.

Constitutive descriptions of hybrid SFRP composites

A micromechanics-based constitutive model is proposed to simulate the overall behaviors of the hybrid SFRP composites. The derived model is based on an ensemble-volume-averaged homogenization procedure presented in Ju and Chen (1994) and Lee and Simunovic (2000), and the progressive damage model of short fiber described in Pyo and Lee (2009). In contrast to the earlier studies (Khan et al., 2011; Lee and Simunovic, 2000; Pyo and Lee, 2009), a two-level homogenization

process is newly proposed in the present study to model the unique properties of the hybrid SFRP composites (Figure 1(b)).

The first homogenization approach considers the progressive multi-level damage and the presence of air void, and treats the epoxy resin (phase 0), GF (glass fiber) with different levels of damage (phases 1, 2, 3, and 4) and void (phase 5) as a single matrix (phase SFRP) (Yang et al., 2014). The progressive damage model is expressed in terms of the volume fraction of GF, as in previous studies (Pyo and Lee, 2009; Yang et al., 2014). The effective stiffness tensor of the SFRP composites, denoted by $<C^*_{SFRP}>$, consisting of two-dimensional (2D) randomly oriented discontinuous GF and void can be derived as follows (Ju and Sun, 2001; Yang et al., 2014).

$$\left\langle C^*_{SFRP} \right\rangle = \frac{1}{\pi} \int_0^\pi a_{ip} a_{jq} a_{kr} a_{ls} \left(C_{ijkl} \right)^*_{SFRP} \mathrm{d}\theta = \hat{C}^{(1)}_{PR} \delta_{pq} \delta_{rs} + \hat{C}^{(2)}_{PQ} \left(\delta_{pr} \delta_{qs} + \delta_{ps} \delta_{qr} \right) \tag{1}$$

In equation (1), $<\cdot>$ denotes the 2D orientational average process and the second-rank tensors, and the constants $\hat{C}^{(1)}_{IK}$ and $\hat{C}^{(2)}_{IJ}$ are given in the Appendix B of Yang et al. (2014). A more detailed description on the damage model for random-chopped SFRP composites can be found in Yang et al. (2014).

The effective stiffness tensor of the hybrid SFRP composites C^*_{hybrid} then undergoes the second homogenization of the composites. In the second homogenization process, the hybrid SFRP composites are assumed to consist of an anisotropic SFRP matrix and unidirectionally aligned, yet randomly located cylindrical CFs, as shown in Figure 1(b). In addition, the debonding damage between an SFRP matrix and CF cores is not considered in the second homogenization level. Thus, the overall elastic behaviors of the two-phase composites consisting of an SFRP matrix and CF cores are modeled in the formulation. The computational iteration and calculation process of the proposed model for the hybrid SFRP composites are presented in Figure 2. Hence, the stiffness tensor C^*_{hybrid} of the CF cores-embedded SFRP composites can be estimated as (cf., Ju and Chen, 1994; Lee et al., 2005)

$$C^*_{hybrid} = \left\langle C^*_{SFRP} \right\rangle \cdot \left[I + \phi_{cf} (S^{cf} + \tilde{A}_1)^{-1} \cdot \left\{ I - S^{cf} \cdot \phi_{cf} \left(S^{cf} + \tilde{A}_1 \right)^{-1} \right\}^{-1} \right] \tag{2}$$

with

$$\tilde{A}_1 \equiv \left[\tilde{C}_1 - \left\langle C^*_{SFRP} \right\rangle \right]^{-1} \cdot \left\langle C^*_{SFRP} \right\rangle \tag{3}$$

where I is the fourth-rank identity tensor, $\tilde{C}_1$ and ϕ_{cf} are the elasticity tensor and volume fraction of the CF cores, and the tilde ($\sim$) denotes the parameters associated with the CF, respectively. The interior-point Eshelby tensor S^{cf} for cylindrical fibers embedded in and perfectly bonded with an infinite matrix can be expressed as (Ju and Ko, 2008; Sun and Ju, 2004)

$$S^{cf} = \frac{1}{4(1 - \nu_0)} \left\{ \tilde{S}^{(1)}_{IK} \delta_{ij} \delta_{kl} + \tilde{S}^{(2)}_{IJ} \left(\delta_{ik} \delta_{jl} + \delta_{il} \delta_{jk} \right) \right\} \tag{4}$$

in which

$$\tilde{S}^{(1)}_{11} = \tilde{S}^{(1)}_{22} = \tilde{S}^{(1)}_{12} = \tilde{S}^{(1)}_{21} = \frac{1}{2} \left(4\nu^*_{SFRP} - 1 \right), \quad \tilde{S}^{(1)}_{13} = \tilde{S}^{(1)}_{23} = 2\nu^*_{SFRP},$$

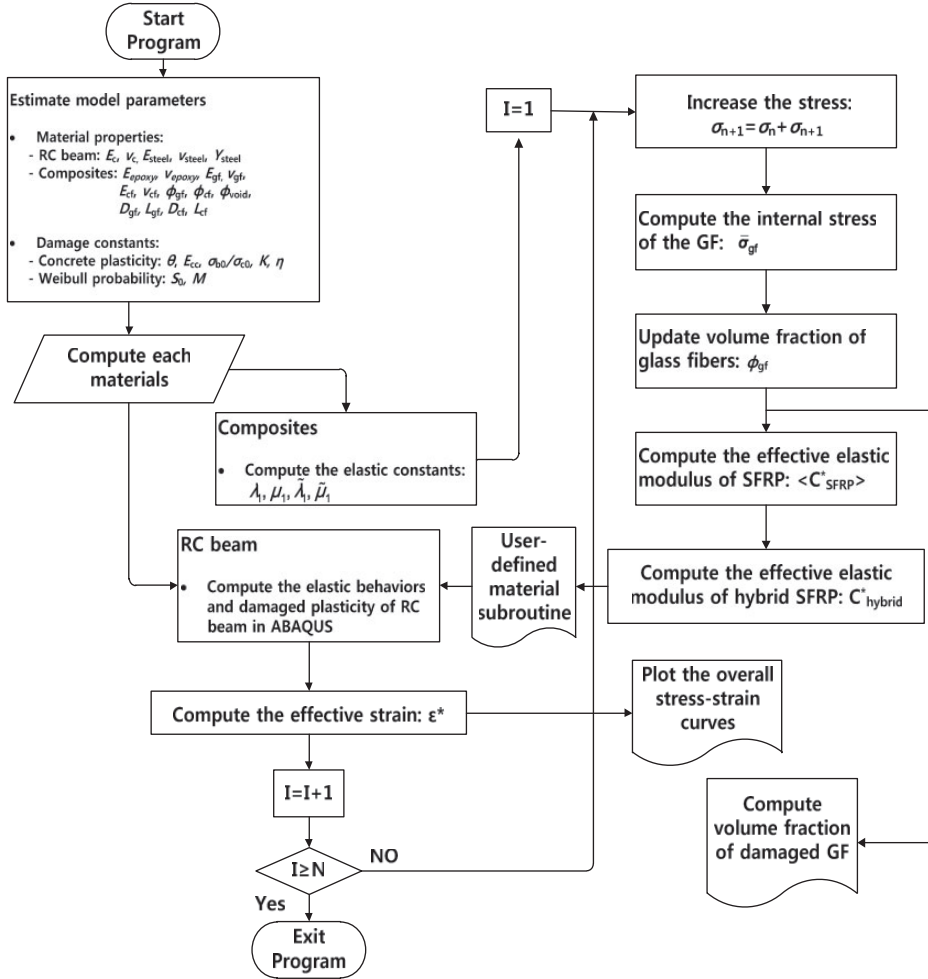**Figure 2.** The computational iteration and calculation process flow of the present modeling for hybrid SFRP composites.

$$\tilde{S}^{(1)}_{31} = \tilde{S}^{(1)}_{32} = \tilde{S}^{(1)}_{33} = 0, \quad \tilde{S}^{(2)}_{11} = \tilde{S}^{(2)}_{22} = \tilde{S}^{(2)}_{12} = \tilde{S}^{(2)}_{21} = \frac{1}{2}\left(3 - 4v^*_{SFRP}\right),$$

$$\tilde{S}^{(2)}_{11} = \tilde{S}^{(2)}_{22} = \tilde{S}^{(2)}_{12} = \tilde{S}^{(2)}_{21} = \frac{1}{2}\left(3 - 4v^*_{SFRP}\right),$$

$$\tilde{S}^{(2)}_{13} = \tilde{S}^{(2)}_{23} = \tilde{S}^{(2)}_{31} = \tilde{S}^{(2)}_{32} = \left(1 - v^*_{SFRP}\right), \quad \tilde{S}^{(2)}_{33} = 0 \tag{5}$$

where v^*_{SFRP} denotes the Poisson's ratio of SFRP composites. By adopting the Eshelby tensor, the effective elasticity tensor for the hybrid SFRP composites containing CF cores can be derived as

$$\tilde{C}^*_{hybrid} = \left\{ \tilde{C}^{(1)}_{IK}\delta_{ij}\delta_{kl} + \tilde{C}^{(2)}_{IJ}\left(\delta_{ik}\delta_{jl} + \delta_{il}\delta_{jk}\right) \right\} \tag{6}$$

in which

$$\tilde{\mathbf{C}}_{IK}^{(1)} = \left[2\hat{C}_{IK}^{(1)}\Gamma_{KK}^{(2)} + 2\hat{C}_{II}^{(2)}\Gamma_{IK}^{(1)} + \sum_{R=1}^{3} \hat{C}_{IR}^{(1)}\Gamma_{RK}^{(1)} \right], \quad \tilde{\mathbf{C}}_{IJ}^{(2)} = \left[\hat{C}_{IJ}^{(2)}\Gamma_{IJ}^{(2)} + \hat{C}_{IJ}^{(2)}\Gamma_{JI}^{(2)} \right] \tag{7}$$

with

$$\Gamma_{IK}^{(1)} = 2B_{IK}^{(1)}N_{KK}^{(2)} + 2B_{II}^{(2)}N_{IK}^{(1)} + \sum_{R=1}^{3} B_{IR}^{(1)}N_{RK}^{(1)}, \quad \Gamma_{IJ}^{(2)} = B_{IJ}^{(2)}N_{IJ}^{(2)} + B_{IJ}^{(2)}N_{JI}^{(2)} \tag{8}$$

and

$$N_{IK}^{(1)} = -\frac{\Omega_{IK}}{2N_{II}^{(4)}}, \quad N_{IJ}^{(2)} = \frac{1}{4N_{II}^{(4)}} \tag{9}$$

with

$$\begin{Bmatrix} \Omega_{I1} \\ \Omega_{I2} \\ \Omega_{I3} \end{Bmatrix} = \begin{bmatrix} N_{11}^{(3)} + 2N_{11}^{(4)} & N_{21}^{(3)} & N_{31}^{(3)} \\ N_{12}^{(3)} & N_{22}^{(3)} + 2N_{22}^{(4)} & N_{32}^{(3)} \\ N_{13}^{(3)} & N_{23}^{(3)} & N_{33}^{(3)} + 2N_{33}^{(4)} \end{bmatrix}^{-1} \begin{Bmatrix} N_{I1}^{(3)} \\ N_{I2}^{(3)} \\ N_{I3}^{(3)} \end{Bmatrix} \tag{10}$$

where the parameters $N_{IK}^{(3)}$ and $N_{IJ}^{(4)}$ can be defined as

$$N_{IK}^{(3)} = \frac{1}{4(1 - v_0)} \left[2S_{IK}^{(1)}B_{KK}^{(2)} + 2S_{II}^{(2)}B_{IK}^{(1)} + \sum_{R=1}^{3} S_{IR}^{(1)}B_{RK}^{(1)} \right]$$

$$N_{IJ}^{(4)} = \frac{1}{2} - \frac{1}{4(1 - v_0)} \left[S_{IJ}^{(2)}B_{IJ}^{(2)} + S_{IJ}^{(2)}B_{JI}^{(2)} \right] \tag{11}$$

in which

$$B_{IK}^{(1)} = -\frac{\phi_{cf}T_{IK}}{2\Lambda_{II}^{(2)}}, \quad B_{IJ}^{(2)} = \frac{\phi_{cf}}{4\Lambda_{IJ}^{(2)}} \tag{12}$$

with

$$\begin{Bmatrix} T_{I1} \\ T_{I2} \\ T_{I3} \end{Bmatrix} = \begin{bmatrix} \Lambda_{11}^{(1)} + 2\Lambda_{11}^{(2)} & \Lambda_{21}^{(1)} & \Lambda_{31}^{(1)} \\ \Lambda_{12}^{(1)} & \Lambda_{22}^{(1)} + 2\Lambda_{22}^{(2)} & \Lambda_{32}^{(1)} \\ \Lambda_{13}^{(1)} & \Lambda_{23}^{(1)} & \Lambda_{33}^{(1)} + 2\Lambda_{33}^{(2)} \end{bmatrix}^{-1} \begin{Bmatrix} \Lambda_{I1}^{(1)} \\ \Lambda_{I2}^{(1)} \\ \Lambda_{I3}^{(1)} \end{Bmatrix} \tag{13}$$

in which

$$\Lambda_{IK}^{(1)} = 2\Lambda_{IK}^{(3)}\hat{C}_{KK}^{(2)} + 2\Lambda_{II}^{(4)}\hat{C}_{IK}^{(1)} + \sum_{R=1}^{3} \Lambda_{IR}^{(3)}\hat{C}_{RK}^{(1)} + \frac{S_{IK}^{(1)}}{4(1 - 2v_0)}$$

$$\Lambda_{IJ}^{(2)} = \Lambda_{IJ}^{(4)}\hat{C}_{IJ}^{(2)} + \Lambda_{IJ}^{(4)}\hat{C}_{JI}^{(2)} + \frac{S_{IJ}^{(2)}}{4(1 - 2v_0)} \tag{14}$$

and

$$\Lambda_{IK}^{(3)} = -\frac{Y_{IK}}{2\left(\tilde{\mu}_1 - \hat{C}_{II}^{(2)}\right)}, \quad \Lambda_{IJ}^{(4)} = \frac{1}{4\left(\tilde{\mu}_1 - \hat{C}_{IJ}^{(2)}\right)} \tag{15}$$

with

$$\left\{\begin{array}{c} Y_{I1} \\ Y_{I2} \\ Y_{I3} \end{array}\right\} = \begin{bmatrix} \tilde{\lambda}_1 + 2\tilde{\mu}_1 - \hat{C}_{11}^{(1)} - 2\hat{C}_{11}^{(2)} & \tilde{\lambda}_1 - \hat{C}_{21}^{(1)} & \tilde{\lambda}_1 - \hat{C}_{31}^{(1)} \\ \tilde{\lambda}_1 - \hat{C}_{12}^{(1)} & \tilde{\lambda}_1 + 2\tilde{\mu}_1 - \hat{C}_{22}^{(1)} - 2\hat{C}_{22}^{(2)} & \tilde{\lambda}_1 - \hat{C}_{32}^{(1)} \\ \tilde{\lambda}_1 - \hat{C}_{13}^{(1)} & \tilde{\lambda}_1 - \hat{C}_{23}^{(1)} & \tilde{\lambda}_1 + 2\tilde{\mu}_1 - \hat{C}_{33}^{(1)} - 2\hat{C}_{33}^{(2)} \end{bmatrix}^{-1}$$
$$\cdot \left\{\begin{array}{c} \tilde{\lambda}_1 - \hat{C}_{I1}^{(1)} \\ \tilde{\lambda}_1 - \hat{C}_{I2}^{(1)} \\ \tilde{\lambda}_1 - \hat{C}_{I3}^{(1)} \end{array}\right\} \tag{16}$$

where $\tilde{\lambda}_1$ and $\tilde{\mu}_1$ are the Lamé constants of the CF. Based on the stiffness matrix of the hybrid SFRP (transversely isotropic), the stress-strain relationship can be expressed as

$$\begin{pmatrix} \sigma_{11} \\ \sigma_{22} \\ \sigma_{33} \\ \sigma_{23} \\ \sigma_{13} \\ \sigma_{12} \end{pmatrix} = \begin{bmatrix} \tilde{C}_{11}^{(1)} + 2\tilde{C}_{11}^{(2)} & \tilde{C}_{12}^{(1)} & \tilde{C}_{13}^{(1)} & 0 & 0 & 0 \\ \tilde{C}_{21}^{(1)} & \tilde{C}_{22}^{(1)} + 2\tilde{C}_{22}^{(2)} & \tilde{C}_{23}^{(1)} & 0 & 0 & 0 \\ \tilde{C}_{31}^{(1)} & \tilde{C}_{32}^{(1)} & \tilde{C}_{33}^{(1)} + 2\tilde{C}_{33}^{(2)} & 0 & 0 & 0 \\ 0 & 0 & 0 & \tilde{C}_{23}^{(2)} & 0 & 0 \\ 0 & 0 & 0 & 0 & \tilde{C}_{13}^{(2)} & 0 \\ 0 & 0 & 0 & 0 & 0 & \tilde{C}_{12}^{(2)} \end{bmatrix} \begin{pmatrix} \varepsilon_{11} \\ \varepsilon_{22} \\ \varepsilon_{33} \\ 2\varepsilon_{23} \\ 2\varepsilon_{13} \\ 2\varepsilon_{12} \end{pmatrix} \tag{17}$$

Experimental study

Materials

The mix proportion and fresh state property of concrete used in this study are summarized in Table 1. Portland cement belonging to Type I specified in ASTM C150 (ASTM, 2012) was used. Crushed gravel with a maximum nominal size of 25 mm and river sand were used as coarse and fine aggregate, respectively. Cylindrical concrete specimens with sizes of 100×200 mm (diameter $\times$ height) were cast to measure the compressive strength and elastic modulus of the RC beams. The specimens were cured for 28 days at a temperature of $20°C$ and relative humidity of 90%. The measured compressive strength and elastic modulus of the concrete are shown in Table 2. The compressive strength and elastic modulus of the concrete were 44.7 MPa and 31.4 GPa, respectively, on average, and the measured error was 3.16% and 1.58%, respectively. The measured test data of cylindrical concrete specimens were applied to FE simulations for modeling the reduced stiffness of concrete as crack propagates in the concrete (Genikomsou and Polak, 2015).

Rectangular concrete beams with sizes of $100 \times 100 \times 400$ mm (width $\times$ height $\times$ length) for three-point bending tests were also fabricated in accordance with ASTM C 293 (ASTM, 2005). The steel bar was embedded at 25 mm away from the concrete bottom. The yield strength and elastic modulus of the steel bar (D6) were 361 MPa and 210 GPa, respectively.

Table 1. Mix proportion of concrete.

Gmax* (mm)	Slump (cm)	w/c (%)	s/a** (%)	Unit weight (kg/m³)				
				Water	Cement	Sand	Coarse aggregate	Super-plasticizer
25	15 ± 2.50	46.64	74.80	176	391	754	1008	2.27

*Maximum aggregate size.
**Sand to coarse aggregate ratio.

Table 2. Measured compressive strength and elastic modulus of concrete.

Specimen	Compressive strength (MPa)	Elastic modulus (GPa)
No. 1	46.4	32.0
No. 2	43.0	30.8
No. 3	44.8	31.5
Mean	44.7	31.4
Std. dev.	1.42	0.50
Coefficient of variance (%)	3.16	1.58

Table 3. Properties of materials used for the fabrication of hybrid SFRP composites.

	Tensile strength (MPa)	Elastic modulus (GPa)	Poisson's ratio	Specific gravity	Diameter (μm)
Carbon fiber	3500	240	0.28	1.76	7
Glass fiber*	2700-3700	7.25	0.2	1.30	11
Epoxy*	55	1.3	0.3	1.09	–

*cf. Ha et al.(2015a,b).

For the fabrication of the hybrid SFRP composites, CF (manufactured by Aksa Co., Ltd, by the product name of A-35 6K 400 TEX), GF (manufactured by Owens Corning, by the product name of ME3023-2400TEX), and epoxy resin (manufactured by Noroo Paint & Coating Co., Ltd., bisphenol A type base epoxy resin and modified amine) were used. The properties of these materials are provided in Table 3.

Experimental process

The experimental plan was designed to investigate the effect of CF cores on the strengthening performance of the hybrid SFRP composite. Specifically, the structural and failure behavior of the RC beams strengthened with the hybrid SFRP composites containing 0, 3, and 9 CF cores were examined, as summarized in Table 4.

The RC beams were strengthened with the hybrid SFRP composites by following the procedure in Figure 3 and Table 5. After 28 days of curing, the bottom face of the RC beams was grinded to remove laitance. The geometry of the strengthening area was marked and taped around in order

Table 4. Summary of test plan.

	Volume fraction of GF (%)	Composite thickness (mm)	Composite dimension (mm)	No. of CF core	Area ratio of core relative to whole composite (%)
Control	0	0	0	0	0
0C	25	4	300×50	0	0
3C	25	4	300×50	3	0.35
9C	25	4	300×50	9	1.04
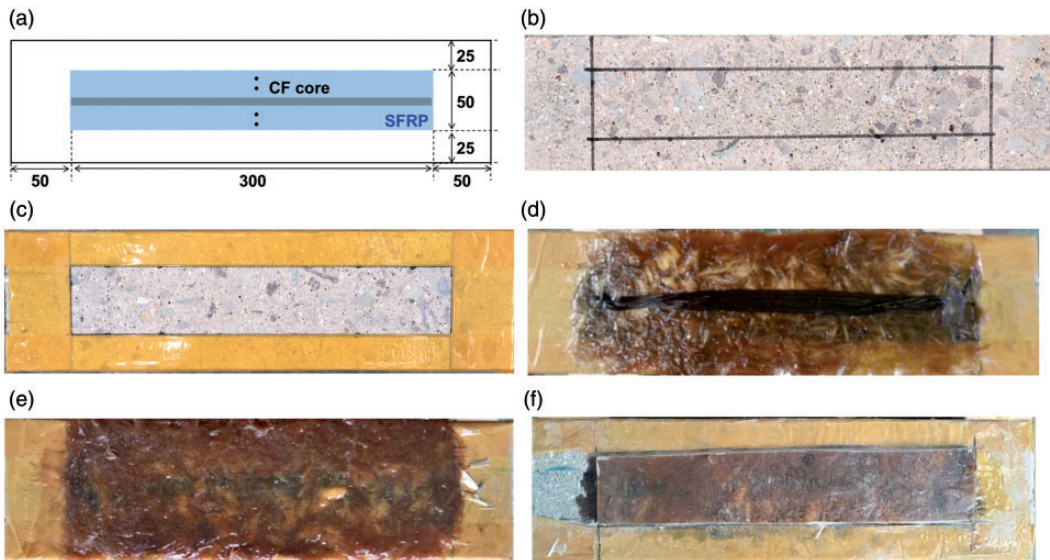
Figure 3. Procedure of strengthening a reinforced concrete beam with hybrid SFRP composites. (a) Geometry of the hybrid SFRP composites bonded to the concrete substrate, strengthening procedure: (b) marking the strengthening area (c) taping around the strengthening area and drilling anchor holes for those with a core, (d) lay-up of SFRP and installing a core along the beam and through the anchor holes, (e) lay-up of the final layer of SFRP, and (f) cutting the edge of the strengthening area.

to easily remove the coating outside the strengthening area. Then, the multiple layup process of SFRP proposed by Ha et al. (2015a) was applied with slight modification to include the installation of the CF cores in the middle of SFRP layers (Table 5). The deposited weight of epoxy resin and chopped GF of 15 mm in length for each layer of SFRP was calculated using the method proposed by Ha et al. (2015a), to reach the target thickness of 4 mm. The epoxy resin was first applied on the concrete substrate, the chopped fibers were randomly distributed by hand, and then roll-out work was conducted to complete one layer of SFRP. After the second layer was complete, the CF cores were laid along the beam. The RC beams strengthened with the hybrid SFRP composites were cured for another 14 days before testing.

The experimental setup of a three-point bending test for a typical RC beam strengthened with the hybrid SFRP composites is shown in Figure 4. The three-point bending tests were conducted on a Universal Testing Machine (UTM) using a 500 kN load cell at a loading rate of 0.015 mm/s

Table 5. Multi layup process of hybrid SFRP composites (cf. Ha et al., 2015a).

No. of layer	Lay-up process	Deposited weight (g)	
		Epoxy resin	Chopped fibers
1st	Epoxy resin + chopped fibers	24.4	38.3
	Roll-out work	–	–
2nd	Epoxy resin + chopped fibers	24.4	38.3
	Roll-out work	–	–
–	CF core	–	–
3rd	Epoxy resin + chopped fibers	24.4	38.3
	Roll-out work	–	–
4th	Epoxy resin + chopped fibers	24.4	38.3
	Roll-out work	–	–
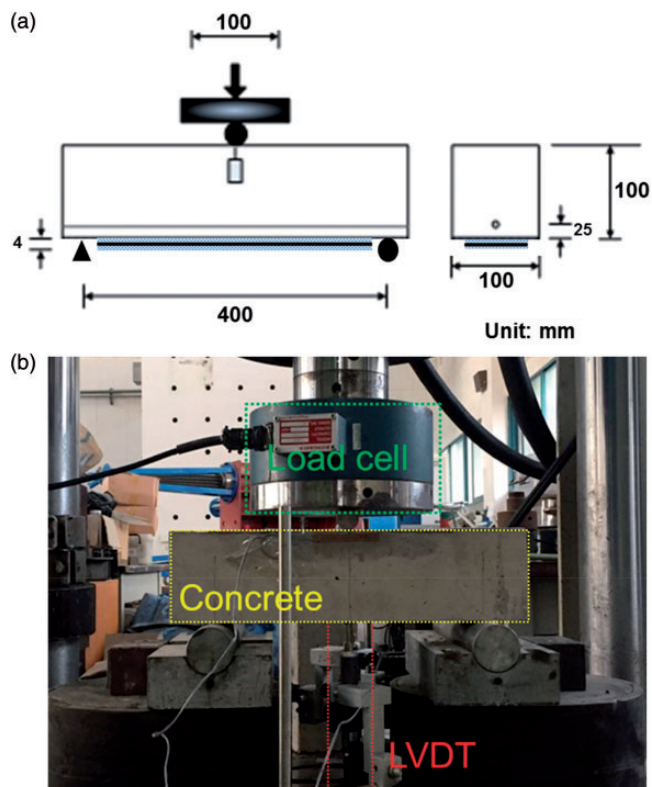
Figure 4. (a) The schematic diagram and (b) the actual setup of the three-point bending test of a typical RC beam strengthened with hybrid SFRP composites.

(cf. Khalid et al., 2015). Two linear variable displacement transducers (LVDTs) were placed below the mid-span to record the vertical displacement induced by the applied load. The data were collected every 0.1 s.

Structural behaviors of experimental tests

The failure mode of the RC beams strengthened with the hybrid SFRP composites observed during the three-point bending tests is shown in Figure 5. The control specimen showed a flexural shear crack at the mid-span propagating from the tension face to the compression face of the beam. Similarly, this behavior was observed in 0C and 3C specimens, containing 0 and 3 CF cores in the SFRP composites, but the difference was that a fracture of the SFRP composites was also
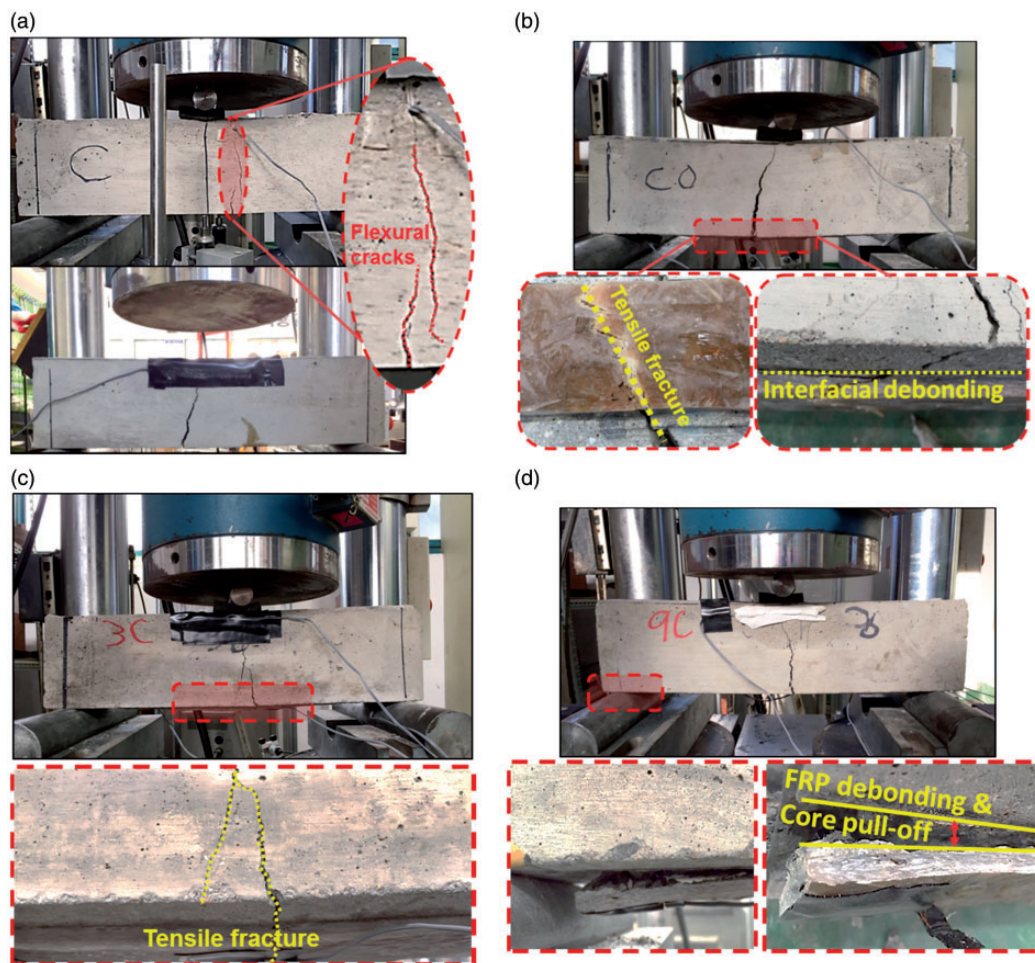

Figure 5. The failure mode of RC beams strengthened with hybrid SFRP composites: (a) control, (b) 0C, (c) 3C, and (d) 9C.
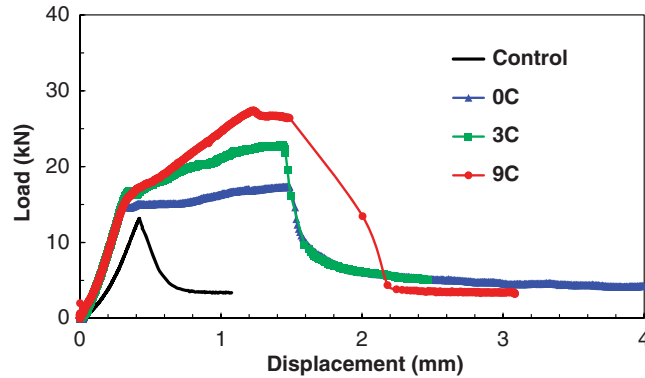
Figure 6. Load-displacement curve of RC beams strengthened with hybrid SFRP composites.

Table 6. The ultimate load, pak displacement, and energy absorption capacity of RC beams strengthened with hybrid SFRP composites.

Specimen	Ultimate load		Peak displacement		Energy absorption capacity	
	Exp. (kN)	Increased ratio (%)	Exp. (mm)	Increased ratio (%)	Exp. (kN·mm)	Increased ratio (%)
Control	14.46	–	0.55	–	7.58	–
0C (0 Core)	17.42	20.5	1.50	172.73	21.77	187.20
3C (3 Cores)	22.88	58.2	1.45	163.64	26.52	249.87
9C (9 Cores)	27.38	89.3	1.24	125.45	38.79	411.74

observed. 9C specimen containing 9 CF cores in the composites, however, showed a different failure mode during the three-point bending test. The crack propagation in the concrete was similar to other specimens, while the core was pulled off and the end of the hybrid SFRP composite layer was peeled off, showing debonding failure.

The load-displacement curves of the RC beams strengthened with the hybrid SFRP composites are shown in Figure 6. The ultimate load, peak displacement, and the energy absorption capacity of the RC beams strengthened with the hybrid SFRP composites obtained from the three-point bending tests are summarized in Table 6. The ultimate load of the RC beams strengthened with the hybrid SFRP composites with 0, 3, and 9 CF cores was 17.42, 22.88, and 27.38 kN, showing an increase by 20.5%, 58.2%, and 89.3%, respectively, relative to that of control. The control specimen showed a typical load-displacement curve of an RC beam under flexural shear failure, without yielding of the embedded steel bar. On the other hand, the RC beams strengthened with the hybrid SFRP composites with 0, 3, and 9 CF cores showed a knee on the load-displacement curve, associated with the yielding of steel bar. In particular, those with 0 and 3 cores showed ductile behavior after the yielding of steel bar, until it failed due to the rupture of the FRP composites at the ultimate load. Meanwhile, the specimen strengthened with hybrid SFRP composites with 9 CF cores showed interfacial crack-induced debonding around the anchorage at the peak load, and the rupture of the FRP composites at the ultimate load.

The energy absorption capacity of the RC beams strengthened with the hybrid SFRP composites displayed a similar trend, showing an increase with the number of CF cores in the composites; specifically, the energy absorption capacity of those containing 0, 3 and 9 CF cores was 21.77, 26.52, and 38.79 kN·mm, showing an increase by 187.20%, 249.87%, and 411.74%, respectively, relative to that of control. Meanwhile, the peak displacement of the RC beams strengthened with the hybrid SFRP composites exhibited a different behavior. The peak displacement of that containing 0, 3, and 9 CF cores was 1.50, 1.45, and 1.24 mm showing an increase by 172.73%, 163.64%, and 125.45%, respectively, relative to that of control. The observed trend showed that the peak displacement decreased with an increasing number of the CF cores.

Numerical simulation of RC beams with hybrid SFRP composites

FE modeling

The derived linear-elastic constitutive equation is implemented into the commercial FE software ABAQUS (ABAQUS, 2016) using a user-defined material subroutine to predict the strengthening effectiveness of the RC beams retrofitted with the hybrid SFRP composites (Lee et al., 2005). In FE simulations, the concrete damaged plasticity (CDP) model, which is based on the modified Drucker-Prager yield function, in ABAQUS is used to simulate the inelastic behavior of concrete under the loading. The CDP model consists of the non-associated hardening plasticity and scalar (isotropic) damage to capture the irreversible damage during the fracturing process. The yield function is defined according to equation (18) (Jankowiak and Lodygowski, 2005; Lee and Fenves, 1998; Lubliner et al., 1988):

$$F = \frac{1}{1-\tau}\left(\bar{q} - 3\tau\bar{p} + \beta(\tilde{\varepsilon}^{pl})\langle\bar{\hat{\sigma}}_{max}\rangle - \gamma\langle-\bar{\hat{\sigma}}_{max}\rangle\right) - \bar{\sigma}_c(\tilde{\varepsilon}^{pl}_c) \tag{18}$$

Moreover, the non-associated potential flow function and the stress-strain relation governed by scalar damage elasticity in concrete are also defined by the following (Genikomsou and Polak, 2015; Lee and Fenves, 1998)

$$G(\sigma) = \sqrt{(\varepsilon\sigma_{t0}\tan\psi)^2 + \bar{q}^2} - \frac{1}{3}I_1\tan\psi \tag{19}$$

and

$$\sigma = (1-d)\bar{\sigma} = (1-d)E_0 : \left(\varepsilon - \varepsilon^{pl}\right) \tag{20}$$

The damage parameters in equation (20) are determined based on the experimental measurements of tensile and compressive stiffness recovery (Genikomsou and Polak, 2015). The details of the aforementioned formulations of the CDP model throughout equations (18) to (20) can be found in Lee and Fenves (1998) and Genikomsou and Polak (2015).

The geometric boundary conditions and FE model with steel bar embedded in the RC beam are shown in Figure 7(a) and (b), respectively. The concrete beam and the hybrid SFRP coating layer are modeled using the eight-node reduced integration solid element (C3D8R), while the two-node
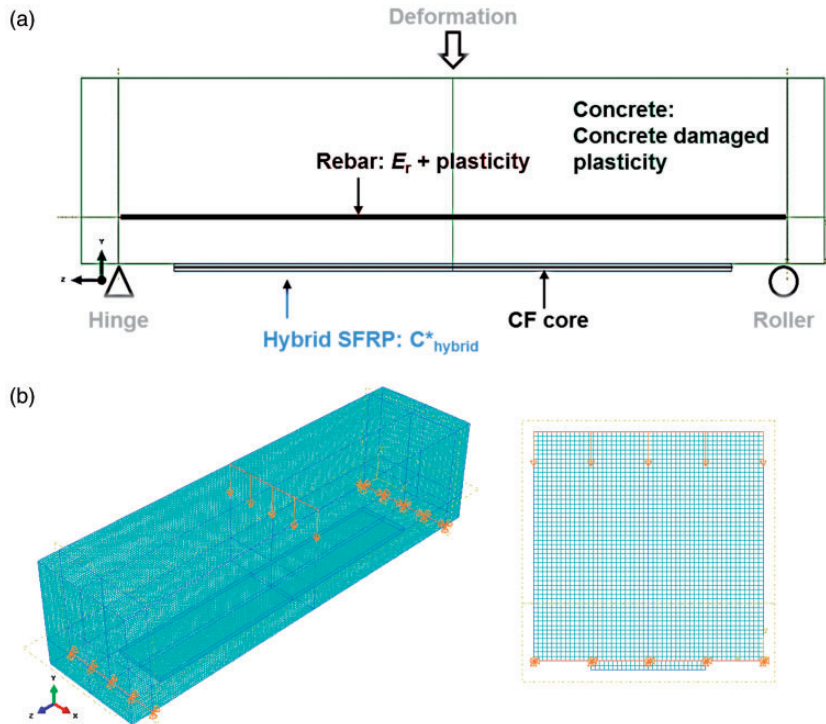
Figure 7. (a) The geometric boundary conditions of a RC beam for three-point bending test and (b) the FE meshes.

linear truss element (T3D2) is used to simulate the rebar in the RC beam (Yang et al., 2015). The loading is applied at the center of the RC beam, identical to the experiment of the present study (Lee et al., 2005).

The material properties of the hybrid SFRP composites used in this simulation are as follows: $E_{\text{epoxy}} = 1.3\,\text{GPa}$, $v_{\text{epoxy}} = 0.3$, $E_{\text{gf}} = 72.5\,\text{GPa}$, $v_{\text{gf}} = 0.2$, $D_{\text{gf}} = 0.155\,\text{mm}$, $L_{\text{gf}} = 15\,\text{mm}$, $E_{\text{cf}} = 240\,\text{GPa}$, $v_{\text{cf}} = 0.28$, $D_{\text{cf}} = 7\,\mu\text{m}$, $L_{\text{cf}} = 300\,\text{mm}$, where E, v, D, and L denote the elastic modulus, Poisson's ratio, diameter and length of materials, respectively. The volume fraction of voids, inevitably included due to the manufacturing nature of SFRP, is assumed to be 10% (Yang et al., 2014). The damage parameters of the 2D randomly oriented GF-reinforced epoxy SFRP composites are selected as $S_0 = 250\,\text{MPa}$ and $M = 0.5$ based on Yang et al. (2014).

In addition, the material properties of RC concrete are as follows: the dilation angle θ was assumed to be 15° from the data for axial and lateral stress-strain in multiaxial state (Chandappa et al. 1999, 2001; Palaniswamy and Shah, 1974). The eccentricity E_{cc} which adjusts the shape of the plane's meridians in the stress space changes can be calculated as a ratio of tensile strength to compressive strength and was assumed to be 0.1. In addition, a ratio of the strength in the biaxial state to the strength in the uniaxial state σ_{b0}/σ_{c0} and the tensile-to-compressive meridian ratio K were assumed to be 1.16 and 0.667, respectively, based on Kupfer and Gerstle (1973) and Chen and Han (1995). The selected parameters of CDP are then implemented in the ABAQUS analyses.
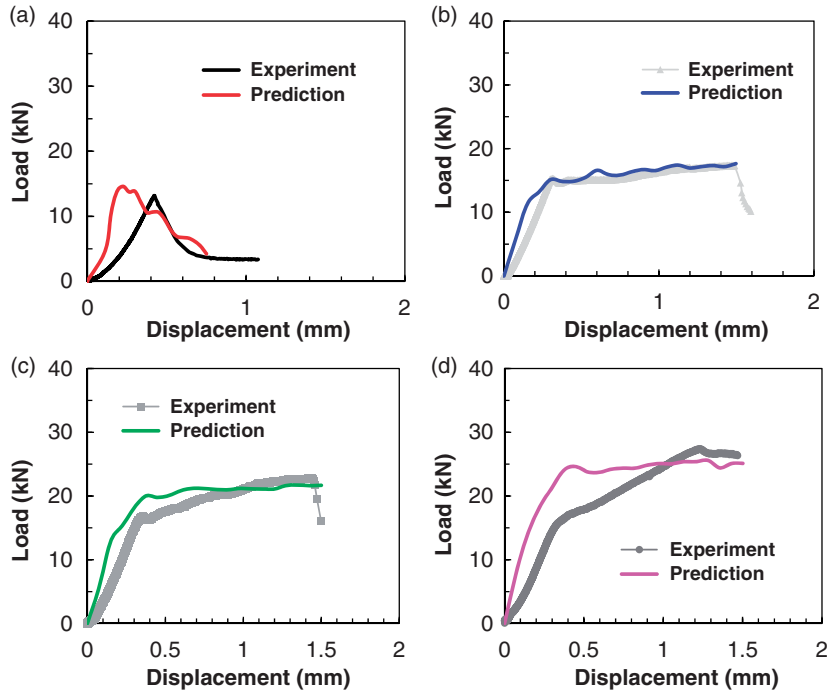
Figure 8. Comparisons of load-displacement curves obtained by the present predictions and experimental data corresponding to (a) the unstrengthened RC beam (control), and those strengthened with (b) 0C, (c) 3C and, (d) 9C.

Comparative study between experimental data and simulation results

The applicability of the present computational model is then assessed by comparing the experimentally obtained load-displacement curve with that predicted by the present model, as shown in Figure 8. Moreover, the behavior RC beam without the composite coating at a loaded state was predicted using the identical model to examine whether this model is applicable to simulating unstrengthened RC beams (i.e. control specimen). The simulated behavior of the RC beams strengthened with the hybrid SFRP composites was in a close proximate to the experimentally observed behavior, showing evidence of the effectiveness of the proposed computational model. The observed divergence from the experiment at higher yield strength in Figure 8(c) and (d) is due to the simulation assumption of perfect bonding between RC beam and composites, in which failure modes such as debonding or rupture of the composites are not considered.

The deformed shape, maximum principle stress, and plastic strain of the beam specimen during the three-point bending simulated in FE are also shown in Figure 9. Strengthening the RC beam with the hybrid SFRP composite was observed to facilitate the reducing maximum principle stress throughout the RC beam and uniform distribution of the load (Figure 9(a)). In addition, the maximum principle plastic strain of the control RC beam and that strengthened with the hybrid SFRP composites is also shown in Figure 9(b). The obtained result was similar to that with the maximum principle stress, showing that strengthening with the hybrid SFRP composites was capable of distributing the plastic strain in the RC beam.
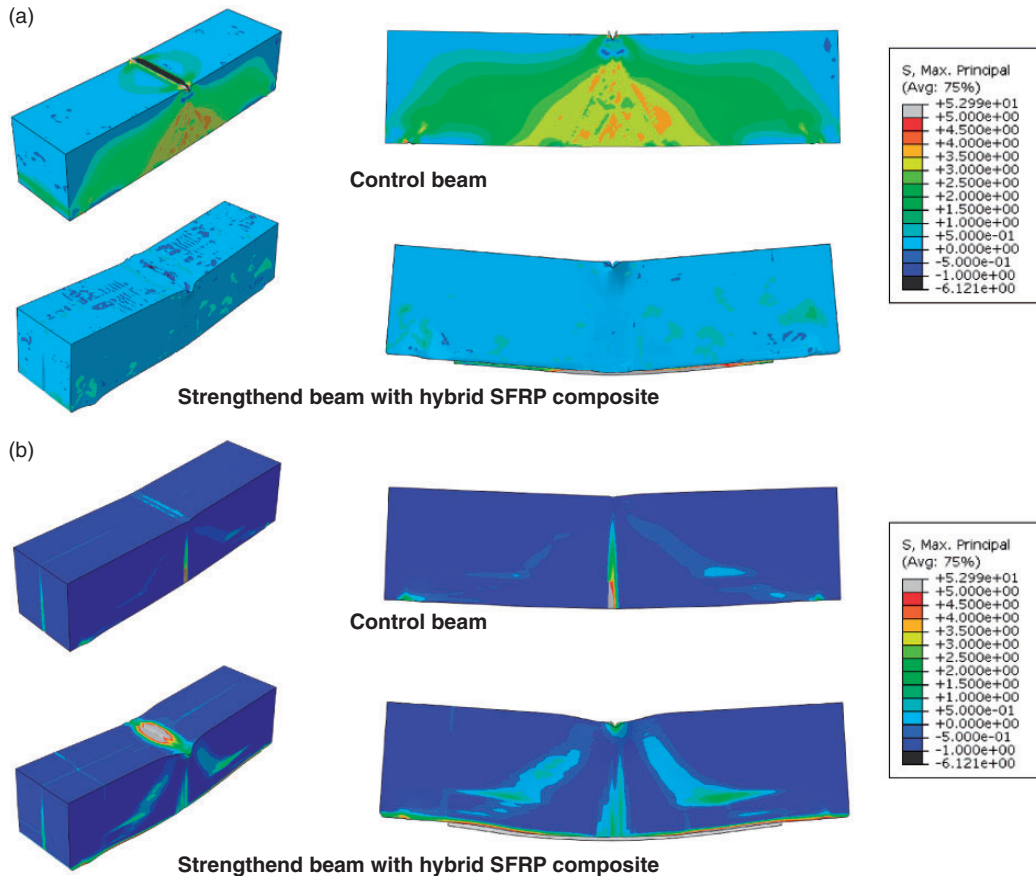
Figure 9. The representative illustrations of (a) maximum principle stress and (b) plastic strain of a control beam and a RC beam strengthened with hybrid SFRP composites during three-point bending tests.

Conclusions

The present study explored the structural strengthening performance of the hybrid SFRP for retrofitting RC beams by means of theoretical and experimental approaches. Material properties of specimens were measured in accordance with related standards, and the model parameters for the simulation were estimated using the obtained experimental results. A micromechanics-based constitutive model for simulating the overall behavior of the hybrid SFRP composites was developed and incorporated in the FE code ABAQUS. The flexural behavior of RC beams strengthened with the hybrid SFRP composites was predicted using the micromechanics and FE methodology for the composites and was compared with the experimental data. The following conclusions can be drawn considering the results of this study:

- The structural behavior of the RC beams strengthened with the hybrid SFRP composites predicted by the theoretical analysis in the present study was in a good agreement with the experimentally observed behavior in the three-point bending tests.

- The ultimate load, peak displacement, and energy absorption capacity of RC beam strengthened with the hybrid SFRP composites were 89.3%, 125.45%, and 411.74% higher than those of the control specimen.
- The behavior of the tested RC beam and specimens with the hybrid SFRP displayed and predicted a typical fracture at the mid-span.
- A marginal variation between the predicted and experimentally observed behavior of RC beams strengthened with the hybrid SFRP under a flexural loading, however, was noted, due mainly to the fact that other damage mechanisms such as delamination and debonding of composites from concrete substrate were not considered.

The proposed theoretical model presented with the experimental validation will broaden the application of the hybrid SFRP composites system for strengthening deteriorated RC beams. Additional series of tests should be followed to explore the strengthening characteristic of the hybrid SFRP composites under different structural constraints. These studies are not limited to, but may include investigation of additional physical characteristics such as debonding properties and viscoelastic behaviors for more realistically predictions of the failure and the strain-rate dependent behavior of the composites (Yang et al., 2012). Nonetheless, these aspects are not of particular scope in the present work and should be considered in future work.

Declaration of Conflicting Interests

Funding

References

ABAQUS (2016) *Analysis User's Manual 6.14*. Providence, RI: Dassault Systems Simulia Corp.

American Society for Testing and Materials (2005) *ASTM C293: Standard Test Method for Flexural Strength of Concrete (Using Simple Beam with Center-Point Loading)*. United States: ASTM International.

American Society for Testing and Materials (2012) *ASTM C150/C150M-12: Standard Specification for Portland Cement*. United States: ASTM international.

Chandappa DC, Sanjayan JG and Setunge S (2001) Complete triaxial stress-strain curves of high strength concrete. *ASCE Journal of Materials in Civil Engineering* 13: 209–215.

Chandappa DC, Setunge S and Sanjayan JG (1999) Stress versus strain relationship of high strength concrete under high later confinement. *Cement and Concrete Research* 29: 1977–1982.

Chen WF and Han DJ (1995) *Plasticity for Structural Engineers*. Taipei: Gau Lih Book Co., Ltd.

Choi DU, Kang THK, Ha SS, et al. (2011) Flexural and bond behavior of concrete beams strengthened with hybrid carbon-glass fiber-reinforced polymer sheets. *ACI Structural Journal* 108: 90–98.

Genikomsou AS and Polak MA (2015) Finite element analysis of punching shear of concrete slabs using damaged plasticity model in ABAQUS. *Engineering Structures* 98: 38–48.

Ha SK, Jang JG, Park SM, et al. (2015a) Advanced spray multiple layup process for quality control of sprayed FRP composites used to retrofit concrete structures. *Journal of Construction Engineering and Management* 141: 04014060.

Ha SK, Khalid HR, Park SM, et al. (2015c) Interfacial crack-induced debonding behavior of sprayed FRP laminate bonded to RC beams. *Composites Structures* 128: 176–187.

Ha SK, Na S, Bang YK, et al. (2015b) An experimental study on sag-resistance ability and applicability of sprayed FRP system on vertical and overhead concrete surfaces. *Materials and Structures* 48: 21–33.

Ha SK, Na S and Lee HK (2013) Bond characteristics of sprayed FRP composites bonded to concrete substrate considering various concrete surface conditions. *Composites Structures* 100: 270–279.

Jankowiak T and Lodygowski T (2005) Identification of parameters of concrete damage plasticity constitutive model. *Foundations of Civil and Environmental Engineering* 6: 53–69.

Ju JW and Chen TM (1994) Micromechanics and effective moduli of elastic composites containing randomly dispersed ellipsoidal inhomogeneities. *Acta Mechanica* 103: 103–121.

Ju JW and Ko YF (2008) Micromechanical elastoplastic damage modeling of progressive interfacial arc debonding for fiber reinforced composites. *International Journal of Damage Mechanics* 17: 307–356.

Ju JW and Sun LZ (2001) Effective elastoplastic behavior of metal matrix composites containing randomly located aligned spheroidal inhomogeneities. Part I: micromechanics-based formulation. *International Journal of Solids and Structures* 38: 183–201.

Kang THK (2016) *Hybridization of Structural Fibers for Synergistic & Ductile Behavior*. Saarbrücken, Germany: Lap Lambert, p. 79.

Kang THK, Kim W, Ha SS, et al. (2014) Hybrid effects of carbon-glass FRP sheets in combination with or without concrete beams. *International Journal of Concrete Structures and Materials* 8: 27–42.

Khalid HR, Ha SK, Park SM, et al. (2015) Interfacial bond behavior of FRP fabrics bonded to fiber-reinforced geopolymer mortar. *Composite Structures* 134: 353–368.

Khan AR, Al-Gadhib AH and Baluch MH (2011) Experimental and computational modeling of low cycle fatigue damage of CFRP strengthened reinforced concrete beams. *International Journal of Damage Mechanics* 20: 211–243.

Kupfer HB and Gerstle KH (1973) Behavior of concrete under biaxial stresses. *ASCE Journal of Engineering Mechanics* 99: 853–866.

Lee HK (2004) Effectiveness of anchorage in concrete beams retrofitted with sprayed fiber-reinforced polymers. *Journal of Reinforced Plastics and Composites* 23: 1285–1300.

Lee HK, Avila G and Montanez C (2005) Numerical study on retrofit and strengthening performance of sprayed fiber reinforced polymer. *Engineering Structures* 27: 1476–1487.

Lee HK and Hausmann LR (2004) Structural repair and strengthening of damaged RC beams with sprayed FRP. *Composite Structures* 63: 201–209.

Lee HK, Hausmann LR and Seaman WC (2008a) Effectiveness of retrofitting damaged concrete beams with sprayed fiber-reinforced polymer coating. *Journal of Reinforced Plastics and Composites* 27: 1269–1286.

Lee HK and Kim BR (2007) Numerical characterization of compressive response and damage evolution in laminated plates containing a cutout. *Composites Science and Technology* 67: 2221–2230.

Lee HK, Kim BR and Ha SK (2008b) Numerical evaluation of shear strengthening performance of CFRP sheets/strips and sprayed epoxy coating repair systems. *Composites Part B: Engineering* 39: 851–862.

Lee HK and Simunovic S (2000) A damage constitutive model of progressive debonding in aligned discontinuous fiber composites. *International Journal of Solids and Structures* 38: 875–895.

Lee J and Fenves GL (1998) Plastic-damage model for cyclic loading of concrete structures. *Journal of Engineering Mechanics* 124: 892–900.

Lubliner J, Oliver J, Oller S, et al. (1988) A plastic-damage model for concrete. *International Journal of Solids and Structures* 25: 299–326.

Nam JW, Kim HJ, Kim SB, et al. (2009) Analytical study of finite element models for FRP retrofitted concrete structure under blast loads. *International Journal of Damage Mechanics* 18: 461–490.

Ouaar A, Doghri I, Delannay L, et al. (2007) Micromechanics of the deformation and damage of steel fiber-reinforced concrete. *International Journal of Damage Mechanics* 16: 227–260.

Palaniswamy R and Shah SP (1974) Fracture and stress-strain relation for concrete under triaxial compression. *ASCE Journal of Structural Engineering* 100: 901–916.

Pyo SH and Lee HK (2009) Micromechanical analysis of aligned and randomly oriented whisker-/short fiber-reinforced composites. *CMES: Computer Modeling in Engineering & Sciences* 40: 271–305.

Sun LZ and Ju JW (2004) Elastoplastic modeling of metal matrix composites containing randomly located and oriented spheroidal particles. *Journal of Applied Mechanics-ASME* 71: 774–785.

Yang BJ, Ha SK, Pyo SH, et al. (2014) Mechanical characteristics and strengthening effectiveness of random-chopped FRP composites containing air voids. *Composites Part B: Engineering* 62: 159–166.

Yang BJ, Kim BR and Lee HK (2012) Predictions of viscoelastic strain-rate dependent behavior of fiber-reinforced polymeric composites. *Composite Structures* 94: 1420–1429.

Yang BJ, Na S, Jang JG, et al. (2015) Thermo-mechanical analysis of road structures used in the on-line electric vehicle system. *Structural Engineering and Mechanics* 53: 519–536.